# Preclinical Comparison of the Amyloid-β Radioligands [11C]Pittsburgh compound B and [18F]florbetaben in Aged APPPS1-21 and BRI1-42 Mouse Models of Cerebral Amyloidosis.

Waldron AM, Verhaeghe J, Wyffels L, Schmidt M, Langlois X, Van Der Linden A, Stroobants S, Staelens S.

Published in Molecular Imaging and Biology

October 2015, Volume 17, Issue 5, pp 688-696

Doi: 10.1007/s11307-015-0833-9

First online: 21 February 2015

**Preclinical comparison of the amyloid-β radioligands [$^{11}$C]-Pittsburgh compound B and [$^{18}$F]-florbetaben in aged APPPS1-21 and BRI1-42 mouse models of cerebral amyloidosis.**

Ann-Marie Waldron[1], Jeroen Verhaeghe[1], Leonie wyffels[1,2], Mark Schmidt[3], Xavier Langlois[3], Annemie Van Der Linden[4], Sigrid Stroobants[2], Steven Staelens[1]*

1. Molecular Imaging Center Antwerp, University of Antwerp, Antwerp, Belgium;

2. Nuclear Medicine, University Hospital Antwerp, Antwerp, Belgium;

3. Department of Neuroscience, Janssen Pharmaceutica NV, Beerse, Belgium;

4. Bio-Imaging Lab, University of Antwerp, Antwerp, Belgium.

***Corresponding author:** Steven Staelens, Molecular Imaging Center Antwerp, University of Antwerp, Campus Drie Eiken – UC**,** Universiteitsplein 1**,** 2610 Wilrijk.

**E-mail:** steven.staelens@uantwerpen.be **Tel:** +32 3 265 2820; **Fax:** +32 3 265 2813

**Running title:** Preclinical comparison of Preclinical comparison of the β-amyloid radioligands [11C]-Pittsburgh compound B and [18F]-florbetaben

**Abstract**

**Purpose:** The aim of this study was to compare [$^{11}$C]- Pittsburgh compound B ([$^{11}$C]-PiB) and [$^{18}$F]-florebtaben ([$^{18}$F]-FBB) for preclinical investigations of amyloid-β pathology.

**Procedures:** We investigated two aged animal models of cerebral amyloidosis with contrasting levels of amyloid-β relating to “high” (APPPS1-21 n= 6, WT n= 7) and “low” (BRI1-42 n=6 , WT n=6 ) target states respectively.

**Results:** APPPS1-21 mice (*high target state*) demonstrated extensive fibrillar amyloid-β deposition that translated to significantly increased retention of [$^{11}$C]-PiB and [$^{18}$F]-FBB in comparison to their wild-type. The retention pattern of [$^{11}$C]-PiB and [$^{18}$F]-FBB in this cohort displayed significant correlation. However the relative difference in tracer uptake between diseased and healthy mice was substantially higher for [$^{11}$C]-PiB than for [$^{18}$F]-FBB. Although immunohistochemistry confirmed the high plaque load in APPPS1-21 mice, correlation between tracer uptake and *ex vivo* quantification of amyloid-β was poor for both tracers. BRI1-42 mice (*low target state*) did not demonstrate increased tracer uptake.

**Conclusions:** In cases of high fibrillar amyloid-β burden both tracers detected significant differences between diseased and healthy mice, with [$^{11}$C]-PiB showing a larger dynamic range.

Keywords: Alzheimer’s, [$^{11}$C]-PiB, [$^{18}$F]-FBB, animal models, small animal imaging

## Introduction

The abnormal accumulation of amyloid-β aggregates, due to the misprocessing of the amyloid precursor protein, is a characteristic pathophysiology of Alzheimer's Disease [1]. With the proposed pathogenic role of amyloid-β, the ability to detect and map the extent of its deposition is an invaluable resource for monitoring disease progression and therapeutic effect. Based on this premise a number of radiotracers targeted against amyloid-β have been developed and allow for an objective and non-invasive measurement of this pathological hallmark with positron emission tomography (PET) [2-3]. A carbon-labeled benzothiazole derivative, [$^{11}$C]-PiB, was the first proposed selective amyloid-β imaging agent [4] and to date is the most extensively studied for both preclinical and clinical applications. Increased [$^{11}$C]-PiB retention has been successfully employed to differentiate between prodromal, AD and healthy individuals [4-5]. Likewise in the preclinical realm, [$^{11}$C]-PiB enables *in vivo* quantification of amyloid-β in transgenic animal models and has been effectively employed to monitor disease progression and measure treatment effect [6-8].

The manifold successes of [$^{11}$C]-PiB spurred the development of fluoro-labeled compounds to overcome the prohibitive half-life of [$^{11}$C] (20 min) and thereby facilitate wider availability and multiple uses of radiotracer productions. These agents include the fluorinated analogue of PiB, ([$^{18}$F]-flutemetamol) [9-11] in addition to compounds derived from other chemical classes such as stilbenes ([$^{18}$F]-florbetapir, [$^{18}$F]-florbetaben) [12-14] and benzofurans ([$^{18}$F]-NAV4694) [15]. These tracers all bind with high affinity to

fibrillar amyloid-β as [$^{11}$C]-PiB [16] and have similarly demonstrated *in vivo* detection of amyloid-β pathology in symptomatic patients and in animal models [17-19]. Despite this congruity, amyloid tracers display different imaging characteristics that arise largely due to their varying degrees of non-specific retention. While high non-specific white matter retention is a shared trait amongst amyloid tracers, it is generally more pronounced with more lipophilic fluoro-labeled compounds and results in lowered signal specificity [20]. Reduced contrast can present issues for the sensitive detection of low pathological burden or small alterations in plaque load and is especially pertinent in small animal imaging where sensitivity is restricted by the limited resolution of PET and the small size of the rodent brain. Based on this premise, the present study aimed to evaluate the sensitivity of [$^{18}$F]-FBB (florbetaben) for preclinical μPET imaging of amyloid-β in relation to the gold standard [$^{11}$C]-PiB. [$^{18}$F]-FBB has many desirable properties for an amyloid tracer, such as rapid *in vivo* uptake, good brain penetration and high affinity for amyloid plaques [12] and has consequently been approved for clinical use.

## 2. Materials and Methods

### *2.1 Animals*

To compare the sensitivity of [$^{18}$F]-FBB and [$^{11}$C]-PiB we investigated two animal models of cerebral amyloidosis with contrasting levels, distribution and subtypes of β-amyloid deposition relating to “high” and “low” tracer target states.

Amyloid tracers bind with high affinity to dense core plaques. For a *high target state* of dense fibrillar amyloid-β burden we employed an aged double transgenic model, APPPS1-21 (n=6) [21].These mice co-express the human Swedish double APP mutation KM670/671NL and the human mutated PS1 L166P driven by the neuron-specific Thy-1 promoter element. Due to these mutations APPPS1-21 mice undergo accelerated and severe disease pathogenesis. Amyloid-β deposition begins as early as 6 weeks of age [21] and at later stages these mice have extensive dense core plaque pathology. Wild-type littermates were used as controls (C57BL6J, n=7).

For a *low target state* we employed aged BRI1-42 mice (n=6). These mice express a BRI-Abeta42 fusion construct under the control of a mouse prion promoter. Human Aβ1-42 is fused to the BRI protein and upon proteolytic cleavage is secreted resulting in extracellular amyloid accumulation. BRI1-42 mice display parenchymal and vascular amyloid deposition starting in the cerebellum (3 months) and later in the forebrain (6 months) [22]. Plaques are predominantly diffuse in nature with dense-core morphology observed almost exclusively in the cerebellum .The combination of relatively modest amyloid burden [23] and diffuse plaque sub-type represent low target abundance for amyloid tracers intrinsically having greater affinity for dense fibrillar plaque. Wild-type littermates were used as controls (B6C3, n=6). All animals were 22-25 months at the time of imaging. We experienced a high drop-out rate of mice, both transgenic and controls, due to the old age of the animals and their sensitivity to extended periods of anesthesia. However, in total 5 mice from the high signal cohort (2 C57Bl6J and 3 APPPS1-21) and 8 mice from the low signal cohort (4 B6C3 and 4

BRI1-42) successfully underwent both scan procedures. Animals that did not survive the first scan were replaced by aged-matched littermates for the second scan to maintain sufficient (n=6) group size. The animals were kept under environmentally controlled conditions (12h light/dark cycle, 20-24°C and 40-70% relative humidity). The study protocol was approved by the local Animal Experimental Ethical Committee of the University of Antwerp, Belgium (2012-25) where the *in vivo* experiments were performed. All animal studies were ethically reviewed and carried out in accordance with European Directive 86/609/EEC Welfare and Treatment of Animals.

*2.2 Tracer radiosynthesis*

[$^{11}$C]-PiB was synthesized in house according to the one step method under neutral conditions. [$^{11}$C]carbon dioxide was produced in an Eclipse HP cyclotron (Siemens, Knoxville) by irradiation of nitrogen (with 2.5% $0_2$). This was then reduced to [$^{11}$C]methane by $H_2$ with an Ni catalyst at 360$^{o}$C in a $^{11}$C alkylation synthesis module (Veestra Instruments, loure Netherlands). Subsequently [$^{11}$C]methyliodide was generated by single pass reaction of [$^{11}$C]methane with $I_2$. The [$^{11}$C]methyliodide was then converted to [$^{11}$C]methyl triflate by passing it over a column consisting of silver trifluoromethanesulfonate impregnated graphitized carbon heated to 180°C. This was then reacted for 3 min with 0.5 mg of precursor (6-OH-BTA-0) dissolved in 250 µl of acetonitrile at 70°C. The reaction mixture was mixed with 0.4 ml of a ethanol and water solution (25/75, v/v) and injected onto a semi- preparative HPLC column (Merck Chromolith SemiPrep RP-18e 10 mm × 100 mm; eluens NaOAc 0.05M pH 5.5/ethanol (60/40, v/v), flow rate 3

ml/min) to isolate the [$^{11}$C]-PIB (retention time ~ 6.2 min). Finally the purified [$^{11}$C]-PIB underwent sterile filtration through a sterile Millipore Millex-GV 0.22 µm filter. [$^{18}$F]-FBB was acquired from BV Cyclotron Amsterdam VU (Amsterdam, The Netherlands) as produced [29].

*2.3 PET Data Acquisition, Reconstruction and Processing*

µPET imaging was conducted using a Siemens Inveon PET/CT system. For all scans anesthesia was induced by inhalation of isoflurane (5% for induction, and 2% for maintenance during preparation and scanning) supplemented with oxygen. Tracers were injected via the tail vein in a fixed volume of 200 µL. During the scan the core body temperature of the animals was maintained via a temperature controlled heating pad. Upon intravenous injection of 7.98 ± 0.62 MBq of [$^{11}$C]-PiB, a 60 min dynamic acquisition was initiated. To exclude the involvement of decreased tracer delivery we conducted dynamic [$^{11}$C]-PiB scans and took the early uptake as a surrogate marker of perfusion. List mode data was originally rebinned into 33 frames following the scheme (12x 10, 3x 20, 3x30, 3x 60, 3x 150, 9x 300). To investigate specific tracer retention after initial uptake list mode data was additionally reframed into (1x 1200, 1x 1800, 1x 600) with the second frame corresponding to 20-50 min scan period taken for analysis. This time frame was determined from the dynamic data to provide the highest contrast between APPPS1-21 and WT mice. In the case of [$^{18}$F]-FBB, tracer administration was again performed via intravenous injection and after a conscious uptake period of 35 min either a 15 or a 25 min scan was acquired depending on the specific activity (and thus injected dose) in order to achieve noise equivalent counts in the images. This protocol was implemented based on a previous preclinical study with [$^{18}$F]-FBB [19] and

with support from in-house data with the closely related stilbene derivative [$^{18}$F]-AV45 (unpublished data). Also, to explore the feasibility of a prolonged uptake period with [$^{18}$F]-FBB scanning as performed in humans, the APPPS1-21 cohort underwent an additional [$^{18}$F]-FBB scan with a 90 min uptake period. All details of imaging protocols are displayed in Table 1.

PET data was reconstructed with two-dimensional ordered subset expectation maximization (OSEM2D)[24] algorithm using 4 subsets and 16 iterations following Fourier rebinning (FORE) [25].The energy and timing window was set to 350-650 keV and 3.432 nsec respectively. The PET images were reconstructed on a 128 x 128 x 159 grid with a pixel size of 0.776 x 0.776 x 0.776 mm. Normalization, dead time, randoms, CT-based attenuation and single scatter stimulation (SSS) [26] corrections were applied. A 5 min CT was acquired subsequent to all PET scans using a 220 degree rotation with 12- rotation steps, voltage and amperage were set to 80 keV and 500 uA respectively.

Volume-of-interest (VOI) analysis was performed on reconstructed images using PMOD v3.3 (PMOD technologies, Switzerland). Individual PET images were first rigidly coregistered with their individual CT sequentially acquired with the aforementioned PET/CT scanners in order to correct for minor motion due to deep anesthesia breathing or bed translation in the gantry from PET to CT. Next, these coregistered PET/CT images were then non-rigidly spatially normalized into the space of a predefined mouse brain MRI/CT template [27] by spatially matching the CT. Thereafter extracerebral activity was removed through the use of a brain mask derived from the T2 weighted MR of the MRI/CT template whereby all voxels outside the brain

mask were set to zero intensity and voxels inside the mask were unaltered. For an absolute measure of tracer uptake, normalized images were scaled according to the percent injected dose (tissue $uptake_{[kBq/cc]}$ / $injected\ dose_{[kBq]}$ * 100). Processed images were subsequently evaluated in a mouse brain VOI template (predefined on the aforementioned MRI/CT template) and tracer uptake values were extracted for each delineated VOI. With this approach regional values are quantified as the average uptake over the total number of voxels in a VOI. To create visual representations of the relative uptake of tracers between diseased and healthy animals, average images were created for each genotype. Thereafter a percent difference image was calculate by the formula $(Mean\_image_{TG} – Mean\_image_{WT}) / (Mean\_image_{WT})*100$.

*2.4 Immunohistochemistry*

After μPET scans, animals were sacrificed and brain tissue was fixed, paraffin- embedded and cut into 5 μm coronal sections. De-waxed and rehydrated sections underwent tissue depigmentation in potassium permanganate, oxalic acid and water and were subsequently pretreated with 70 % formic acid for 10 min for epitope retrieval. Endogenous peroxidase activity was blocked by rinsing in 3 % hydrogen peroxide for 5 min. Thereafter sections were incubated with mouse anti-amyloid primary antibody (JRF/AβN/25 1:15,000 1h), HRP-labeled secondary antibody (anti-mouse, 30 min) and visualized with diaminobenzidine (DAB). Finally the sections were counterstained with hematoxylin, dehydrated by submerging in a series of alcohol, fixed in xylene, mounted and coverslipped.

Virtual images were acquired using a Mirax Digital Slide Scanner (Zeiss) and image analysis was performed using the Definiens analysis software package v1.5. Regions-of-interest (ROIs) were manually delineated in accordance with Franklin and Paxinos atlas [28] and for each ROI the percentage of DAB-labeled area was calculated.

*2.5 Statistical Analysis*

For comparisons of tracer uptake among regions and between transgenic and control animals a two-way, repeated measures ANOVA with post-hoc correction for multiple comparison's (Sidak) was performed. Differences were considered statistically significant if $p < 0.05$. For correlation analysis Pearson's correlation was employed. All statistical analysis was performed in GraphPad Prism v6 software.

## 3. Results

*3.1 Regional amyloid-β deposition and its in vivo detection by μPET scanning.*

*3.1.1 High target state*

As expected for their age and mutations, APPPS1-21 mice demonstrated extensive deposition of amyloid-β by immunohistochemistry (Fig.1a-c). The whole brain was affected with the cortex presenting the highest burden (15.71 ± 3.69 %, Fig.1a). Even the cerebellum, a region without appreciable transgene expression, demonstrated amyloid-β deposition (Fig.1a and 1c), albeit to a much lesser extent than forebrain regions (0.61 ± 0.16 %). Plaques were predominately mature in nature. The pervasive amyloid-β deposition translated to significant retention of both [$^{11}$C]-PiB and [$^{18}$F]-FBB in these mice

in comparison to their WT (Fig.2a and 2b). In the case of [$^{11}$C]-PiB uptake was significantly different in all regions investigated with the striatum and hippocampus (both p= 0.001) revealing the highest significant differences to WT (Fig.2a). [$^{18}$F]-FBB uptake was significantly higher in APPPS1-21 mice in all regions excluding the cerebellum. With [$^{18}$F]-FBB the highest significance was revealed in the cortex and thalamus (both $p < 0.0001$) (Fig.2b). The variance in tracer uptake was smaller with [$^{18}$F]-FBB than for [$^{11}$C]-PiB and thus a higher significance level is reached for all regions. Fig.3 depicts average PET images for [$^{11}$C]-PiB (Fig.3a) and [$^{18}$F]-FBB (Fig.3b) uptake in WT and APPPS1-21 mice.

*3.1.2 Low target state*

Forebrain regions displayed modest diffuse amyloid-β deposition (Fig.1e and 1f) in the range of (0.24 – 1.47 %) (Fig.1d). The cerebellum exhibited the highest amyloid-β burden (4.27 ± 1.39 %) and additionally displayed mature plaque phenotypes (Fig. 1d). Notwithstanding the appreciable amyloid-β deposition in the cerebellum, BRI1-42 mice did not demonstrate notably increased uptake of either [$^{11}$C]-PiB or [$^{18}$F]-FBB in comparison to their WT in any region investigated (Fig.2c and 2d). Fig.3 depicts average PET images for [$^{11}$C]-PiB (Fig.3a) and [$^{18}$F]-FBB (Fig.3b) uptake in WT and BRI1-42 mice.

*3.2 Intra-animal imaging characteristics of [$^{11}$C]-PiB and [$^{18}$F]-FBB in the longitudinal high signal state subset.*

Of the total *high target state* cohort (n=12) the regional uptake and distribution of tracer uptake was compared between a subset of animals (n=5) that had undergone all protocols longitudinally (WT n= 2, APPPS1-21 n =3). In these

five animals that, at this very advanced age, survived both the [$^{11}$C]-PiB and [$^{18}$F]-FBB scans there was a high correlation between regional [$^{11}$C]-PiB and [$^{18}$F]-FBB uptake ($r = 0.89$, $p < 0.0001$) indicating congruent distribution of the amyloid tracers (Fig.4a).

The *in vivo* cerebral distribution of both amyloid tracers showed poor correlation with *ex vivo* measures of amyloid-β (Fig.4b and 4c). In particular, for both tracers there was a notable underestimation of plaque burden in the cortex by μPET measures.

To investigate the difference in contrast obtained for each tracer we measured the percent difference in uptake between APPPS1-21 mice and WT for both [$^{11}$C]-PiB and [$^{18}$F]-FBB. With [$^{11}$C]-PiB relative differences in regional uptake between WT and APPPS1-21 mice were 108 %, 107 %, 114 %, 100 % and 68 % for the striatum, cortex, hippocampus, thalamus and cerebellum respectively. In the same regions, relative differences between genotypes for [$^{18}$F]-FBB were 43 %, 53 %, 45 %, 45 % and 20 % respectively. A visual representation of this comparison is presented in Fig. 5 depicted in percent difference.

## 4. Discussion

μPET imaging of amyloid-β plaques in transgenic mouse models of AD provides an ideal vehicle to assess target engagement of putative anti-amyloid treatments and to non-invasively monitor disease progression. With their greater practicality, fluorinated amyloid tracers are becoming increasingly used over the pioneer [$^{11}$C]-PiB in both clinical and animal research. While clinical data is available regarding the relative sensitivity of these newer

radioligands in comparison to [$^{11}$C]-PiB, animal data comparing amyloid tracers is currently lacking. To this effect, the current study investigated the sensitivity of [$^{18}$F]-FBB in two animal models of cerebral amyloidosis and compared its PET imaging characteristics with that of [$^{11}$C]-PiB in the same cohorts. APPPS1-21 and BRI1-42 transgenic mice were selected to represent *high* and *low target states* in terms of fibrillar amyloid-β load, respectively. In the *high target state* [$^{18}$F]-FBB clearly distinguished diseased animals from controls and demonstrated good regional correlation with [$^{11}$C]-PiB. However [$^{18}$F]-FBB exhibited a lower discriminative power, with [$^{11}$C]-PiB showing higher absolute differences between APPPS1-21 mice and their wild-type. In the *low target state*, neither [$^{18}$F]-FBB nor [$^{11}$C]-PiB demonstrated increased uptake in BRI1-42 transgenic mice. This, taken in addition to the lack of correlation between the obtained µPET signal and *ex vivo* measures of amyloid-β may indicate the limits of accurate detection with *in vivo* imaging in cases of very low or high fibrillar amyloid-β pathology in animal models.

Although [$^{11}$C]-PiB and [$^{18}$F]-FBB thus displayed significant regional correlation, differences emerged in the dynamic range and hence contrast provided between tracers. Relative differences between APPPS1-21 and their WT obtained with [$^{18}$F]-FBB were approximately half that achieved with [$^{11}$C]-PiB. However it should be noted that due to lower variance in tracer uptake the significance obtained between WT and APPPS1-21 mice was higher with [$^{18}$F]-FBB. This is presumably due to the better count statistics obtained with a radiotracer based on [$^{18}$F]. A previous preclinical study found a similarly low contrast whereby only a 14.5 % difference between WT and transgenic mice (5XFAD) was observed with [$^{18}$F]-florbetapir in comparison to a 21 %

difference obtained with [$^{11}$C]-PiB in the same mouse cohort [29]. Clinical comparisons of these fluoro-labeled amyloid tracers to [$^{11}$C]-PiB have yielded analogous results [30-31] with the noted exception of [$^{18}$F]-AZD4694 [32]. As is the case in this study, the cortical distribution of fluoro-labeled tracers correlates well with [$^{11}$C]-PiB but the absolute difference between diseased and healthy subjects is comparatively lower. Specifically for [$^{18}$F]-FBB, a 56 % difference between AD and healthy controls was observed in comparison to a 75 % difference with [$^{11}$C]-PiB [31].

The disparity in imaging characteristics arises from differences in their physiochemical properties and can be attributed in a large part to the increased lipophilicity of fluoro-labeled alternatives [20]. Although this characteristic enhances the brain permeability of a compound, it incurs the cost of increased non-specific binding [33]. [$^{11}$C]-PiB itself suffers from a relatively rapid metabolism [34] and non-specific white matter retention [35] but unlike a number of its [$^{18}$F] counterparts, its metabolism does not yield brain penetrant radiometabolites (except in rat) [36]. In humans, [$^{18}$F]-FBB has an estimated plasma half-life of 6 min and its metabolism produces a number of brain penetrant radiometabolites [37]. Metabolism of [$^{18}$F]-FBB is likely faster in mice, given the generally greater rate of metabolism in rodents. The resultant decrease in signal specificity due to cerebral uptake of both intact tracer and radiometabolites may limit the accuracy of quantification and, as evidenced here, lowers the dynamic range and thus the contrast between diseased and healthy animals. A common method to negate the effects of high non-specific binding is to prolong the uptake time allowing for a longer wash-out period of non-specifically bound tracer. A clinical protocol for [$^{18}$F]-

FBB is based on this premise and involves a 90 min uptake period [31]. We employed a similar protocol in the APPPS1-21 mouse cohort, whereby mice received an i.v injection of [$^{18}$F]-FBB and following a 90 min uptake time, a 15 min static scan was acquired. Results from these scans (Fig.6a) demonstrated extensive accumulation of radioactivity in the skull bone, likely due to defluorination of the tracer. Therefore such an approach is unsuitable for small animal imaging applications. The contribution of non-specific retention to contrast has been described in relation to the binding of [$^{18}$F]-florbetapir in 12 month APPPS1-21 mice [18]. In this study, *ex vivo* autoradiography with [$^{18}$F]-florbetapir evidenced a 60 % difference between WT and transgenic mice in contrast to a 15 % difference obtained with *in vivo* μPET imaging. While the superior results are due in part to the higher resolution of autoradiography they cannot account for this vast difference alone thereby pointing to non-specific retention in vivo.

Although immunohistochemistry confirmed the high plaque load in APPPS1-21, the correlation between regional tracer uptake and regional quantification of amyloid-β was poor for both [$^{11}$C]-PiB and [$^{18}$F]-FBB. With immunohistochemistry the amyloid-β burden observed in the cortex was almost 3-fold higher than that in the striatum, hippocampus and thalamus. However from the μPET data, tracer uptake in the cortex is relatively lower than other forebrain regions. It is likely that the extensive amyloid deposition combined with the small size of the mouse brain precludes accurate quantification due to spillover and partial volume effects (PVE) in these very old APPPS1-21 animals with highly abundant plaque load. In this instance, uptake in the cortex is underestimated due to spillover of activity into adjacent

regions. Indeed in a previous longitudinal investigation of [$^{18}$F]-FBB binding in APP-swe mice, the application of PVE corrections to μPET data resulted in greater cortex to cerebellum uptake values and a higher congruence to *ex vivo* autoradiography and immunohistochemistry measures of plaque load [38]. In addition to PVE, binding of amyloid tracers to white matter [35] or sulfotransferase (SULT1E1) [39] may account for the discrepancies between *in vivo* and *ex vivo* measurements of plaque load.

We evidenced a lack of substantial accumulation of either [$^{18}$F]-FBB or [$^{11}$C]-PiB in aged BRI1-42 mice. Plaques are predominantly diffuse in nature in the forebrain of these mice for which amyloid tracers have lower affinity [40]. Taken in combination with the low amount of amyloid-β, the forebrain may have presented too great a challenge for the tracers to have substantial retention. In contrast to forebrain regions, the dense core plaque pathology evidenced by immunohistochemistry in the cerebellum would be expected to yield an increased *in vivo* signal. However the cerebellum did not demonstrate increased uptake in BRI1-42 mice either in relation to other regions or to their WT. Once more this may be related to reduced sensitivity as a consequence of non-specific retention as outlined previously. The cerebellum has a high content of white matter and thus may be heavily influenced by the effects of high non-specific white matter retention. The spatial resolution of μPET precludes the delineation of white matter tracts in the cerebellum and thus the specific contribution cannot be further investigated. Such enhanced cerebellar uptake has been described in preclinical investigations of [$^{18}$F]-flutemetamol [36]. A secondary issue to consider is the contribution of tracer delivery to the brain. Previous failures to quantify amyloid-β in transgenic models have cited

cerebral blood flow disturbances as a causative factor for lack of specific amyloid tracer binding. This is especially important in BRI1-42 animals, as they develop congophilic amyloid angiopathy [22], which is known to cause disturbances in the cerebral vasculature and may lead to modifications of cerebral blood flow [41]. However analysis of the early time frames from the dynamic [$^{11}$C]-PiB scans in these mice (Fig.6b and Fig.6c) does not support altered perfusion as there were no significant differences in initial uptake between genotypes. Lastly, it has been reported that amyloid plaques in animal models possess fewer high affinity binding sites for amyloid tracers than human plaques due to conformational and compositional differences [7, 42]. In this regard, biochemical differences in plaque composition may account for the lack of tracer binding in BRI1-42 mice in comparison to the significant retention in APPPS1-21 cohort. Such model differences in plaque pathology, in addition to the described sensitivity issues, are the likely cause of early disappointing results with amyloid imaging in animal models [42-43]. Previous studies that investigated multiple models of transgenic mice with the same methodology have also reported differences in *in vivo* tracer binding related to variations in plaque structure. In a longitudinal comparison of [$^{11}$C]-PiB binding in APP23, Tg2576 and APPPS1(dE9) mice, increased tracer binding due to increasing amyloidosis was only observed in APP23 mice [17]. In another comparison of [$^{11}$C]-PiB binding in aging APP23 and APPPS1-21 mice both models demonstrated increasing tracer uptake with worsening amyloidosis [17, 44]. Of interest, while amyloid-β burden in both models was within a similar range, APP23 mice demonstrated a $BP_{ND}$ approximately five times higher than that of APPPS1-21 mice. Both studies concluded that the

relatively large dense-core plaques present in APP23 mice were the underlying source of the higher [$^{11}$C]-PiB binding in comparison to other models [44]. Thus while amyloid imaging is indeed feasible in animal models it is highly dependent on the model employed and the type of plaque pathology at the age of imaging.

Our study into the sensitivity of amyloid tracers is limited in the respect that only a single time point was investigated, and that this time point was an old age with a high pathological burden and additionally a high mortality rate. From our findings we propose that a comparison of [$^{18}$F]-FBB and [$^{11}$C]-PiB in younger APPPS1-21 mice with lower pathological burden would be of interest to further delineate tracer sensitivity.

## 5. Conclusion

There is limited sensitivity of both [$^{11}$C]-PiB and [$^{18}$F]-FBB to detect low levels of fibrillar amyloid-β pathology and diffuse plaques. In cases of high fibrillar amyloid-β burden [$^{11}$C]-PiB and [$^{18}$F]-FBB detected significant differences between diseased and healthy mice, with [$^{11}$C]-PiB showing a larger dynamic range.

## Acknowledgements

The authors are very thankful to Arnold Spaans from the BV Cyclotron VU Amsterdam, The Netherlands) for providing us with the shipments of [$^{18}$F]-FBB and to Philippe Joye and Joke Parthoens (Molecular Imaging Center Antwerp) for technical support with *in vivo* experiments. The authors acknowledge the company KOESLER (Rottenburg, 613 Germany) and Dr.

Mathias Jucker (University of Tubingen) for providing the APPPS1 mice. The BRI mice were obtained from Dr. Samir Kumar-Singh of the Flanders Interuniversity Institute for Biotechnology (VIB), who originally obtained them from the Mayo Foundation for Medical Education and Research. This work was funded by the Agency for Innovation by Science and Technology (IWT), by Antwerp University and Antwerp University Hospital, Belgium. Experimental resources are supported by a research contract (46/FA02006/WP130001) of Antwerp University and Janssen Pharmaceutica and by the European Union's Seventh Framework Programme under Grant agreement no: CP-IP 212043-2 (NAD) and no: 278850 (INMiND). The funding sources had no further role in the study design or in the collection, analysis, and interpretation of the data.

**Conflict of Interest**

The authors report no conflicts of interest.

**6. References**

1. Selkoe DJ (1991) The Molecular Pathology of Alzheimer's. Neuron 6:487-98.

2. Nordberg A (2011) Molecular imaging in Alzheimer's disease: new perspectives on biomarkers for early diagnosis and drug development. Alzheimers Res Ther 3:34.

3. Reiman EM, Jagust WJ (2012) Brain imaging in the study of Alzheimer's disease. Neuroimage 61:505-16.

4. Klunk WE, Engler H, Nordberg A, et al. (2004) Imaging Brain Amyloid in Alzheimer's Disease with Pittsburgh Compound-B. Ann Neurol 55:306-19.

5. Mintun MA, Larossa GN, Sheline YI, et al. (2006) [11C]PIB in a nondemented population: potential antecedent marker of Alzheimer disease. Neurology 67:446-52.

6. Manook A, Yousefi BH, Willuweit A, et al. (2012) Small-animal PET imaging of amyloid-beta plaques with [11C] PiB and its multi-modal validation in an APP/PS1 mouse model of Alzheimer's disease. PLoS One 7:e31310.

7. Maeda J, Ji B, Irie T, et al. (2007) Longitudinal, Quantitative Assessment of Amyloid, Neuroinflammation, and Anti-Amyloid Treatment in a Living Mouse Model of Alzheimer's Disease Enabled by Positron Emission Tomography. J Neurosci 27:10957-68.

8. von Reutern B, Grünecker B, Yousefi BH, Henriksen G, Czisch M, Drzezga A (2013) Voxel-Based Analysis of Amyloid-Burden Measured with [11C]PiB PET in a Double Transgenic Mouse Model of Alzheimer's Disease. Mol Imaging Biol.

9. Nelissen N, Van Laere K, Thurfjell L, et al. (2009) Phase 1 Study of the Pittsburgh Compound B Derivative 18F-Flutemetamol in Healthy Volunteers and Patients with Probable Alzheimer Disease. J Nucl Med 50:1251-59.

10. Rowe CC, Ellis KA, Rimajova M, et al. (2010) Amyloid imaging results from the Australian Imaging, Biomarkers and Lifestyle (AIBL) study of aging. Neurobiol Aging 31:1275-83.

11. Wong DF, Moghekar AR, Rigamonti D, et al. (2013) An in vivo evaluation of cerebral cortical amyloid with [18F]flutemetamol using positron emission tomography compared with parietal biopsy samples in living normal pressure hydrocephalus patients. Mol Imaging Biol 15:230-7.

12. Rowe CC, Ackerman U, Browne W, et al. (2008) Imaging of amyloid β in Alzheimer's disease with18F-BAY94-9172, a novel PET tracer: proof of mechanism. The Lancet Neurology 7:129-35.

13. Clark CM, Pontecorvo MJ, Beach TG, et al. (2012) Cerebral PET with florbetapir compared with neuropathology at autopsy for detection of neuritic amyloid-beta plaques: a prospective cohort study. The Lancet Neurology 11:669-78.

14. Wong DF, Rosenberg PB, Zhou Y, et al. (2010) In vivo imaging of amyloid deposition in Alzheimer disease using the radioligand 18F-AV-45 (florbetapir [corrected] F 18). J Nucl Med 51:913-20.

15. Cselenyi Z, Jonhagen ME, Forsberg A, et al. (2012) Clinical Validation of 18F-AZD4694, an Amyloid-b -Specific PET Radioligand. J Nucl Med 53:415-24.

16. Ni R, Gillberg PG, Bergfors A, Marutle A, Nordberg A (2013) Amyloid tracers detect multiple binding sites in Alzheimer's disease brain tissue. Brain 136:2217-27.

17. Snellman A, Lopez-Picon FR, Rokka J, et al. (2013) Longitudinal Amyloid Imaging in Mouse Brain with 11C-PIB: Comparison of APP23,

Tg2576, and APPswe-PS1dE9 Mouse Models of Alzheimer Disease. J Nucl Med 54:1434-41.

18. Poisnel GG, Dhilly MM, Moustié OO, et al. (2012) PET imaging with [18F]AV-45 in an APP/PS1-21 murine model of amyloid plaque deposition. Neurobiol Aging 33:2561-71.

19. Rominger A, Brendel M, Burgold S, et al. (2013) Longitudinal Assessment of Cerebral beta-Amyloid Deposition in Mice Overexpressing Swedish Mutant beta-Amyloid Precursor Protein Using 18F-Florbetaben PET. J Nucl Med 54:1127-34.

20. Kepe V, Moghbel MC, Långström B, et al. (2013) Amyloid-β positron emission tomography imaging probes: a critical review. J Alzheimers Dis 36:613-31.

21. Radde R, Bolmont T, Kaeser SA, et al. (2006) Aβ42-driven cerebral amyloidosis in transgenic mice reveals early and robust pathology. EMBO reports 7:940-46.

22. McGowan E, Pickford F, Kim J, et al. (2005) Aβ42 Is Essential for Parenchymal and Vascular Amyloid Deposition in Mice. Neuron 47:191-99.

23. Levites Y, Smithson LA, Price RW, et al. (2006) Insights into the mechanisms of action of anti-Abeta antibodies in Alzheimer's disease mouse models. The FASEB Journal 20:2576-78.

24. Hudson HM, Larkin RS (1994) Accelerated image reconstruction using ordered subsets of projection data. IEEE Trans Med Imaging 13:601-09.

25. Defrise M, Kinahan PE, Townsend DW, Michel C, Sibomana M, Newport DF (1997) Exact and approximate rebinning algorithms for 3-D PET data. IEEE Trans Med Imaging 16:145-58.

26. Watson CC (2000) New, faster, image-based scatter correction for 3D PET. IEEE Trans Nucl Sci 47:1587-94.

27. Mirrione MM, Schiffer WK, Fowler JS, Alexoff DL, Dewey SL, Tsirka SE (2007) A novel approach for imaging brain-behavior relationships in mice reveals unexpected metabolic patterns during seizures in the absence of tissue plasminogen activator. Neuroimage 38:34-42.

28. Franklin KB, Paxinos G (1997) Mouse brain in stereotaxic coordinates.

29. Rojas S, Herance JR, Gispert JD, et al. (2013) In vivo evaluation of amyloid deposition and brain glucose metabolism of 5XFAD mice using positron emission tomography. Neurobiol Aging 34:1790-98.

30. Landau SM, Breault C, Joshi AD, et al. (2013) Amyloid-b Imaging with Pittsburgh Compound B and Florbetapir: Comparing Radiotracers and Quantification Methods. J Nucl Med 54:70-77.

31. Villemagne VL, Mulligan R, Pejoska S, et al. (2012) Comparison of 11C-PiB and 18F-florbetaben for Aβ imaging in ageing and Alzheimer's disease. Eur J Nucl Med Mol Imaging 39:983-89.

32. Rowe CC, Pejoska S, Mulligan RS, et al. (2013) Head-to-Head Comparison of 11C-PiB and 18F-AZD4694 (NAV4694) for b -Amyloid Imaging in Aging and Dementia. J Nucl Med 54:880-86.

33. Pike VW (2009) PET radiotracers: crossing the blood–brain barrier and surviving metabolism. Trends Pharmacol Sci 30:431-40.

34. Price JC, Klunk WE, Lopresti BJ, et al. (2005) Kinetic modeling of amyloid binding in humans using PET imaging and Pittsburgh Compound-B. J Cereb Blood Flow Metab 25:1528-47.

35. Fodero-Tavoletti MT, Rowe CC, McLean CA, et al. (2009) Characterization of PiB binding to white matter in Alzheimer disease and other dementias. J Nucl Med 50:198-204.

36. Snellman A, Rokka J, Lopez-Picon FR, et al. (2012) Pharmacokinetics of [18F]flutemetamol in wild-type rodents and its binding to beta amyloid deposits in a mouse model of Alzheimer's disease. Eur J Nucl Med Mol Imaging 39:1784-95.

37. Patt M, Schildan A, Barthel H, et al. (2010) Metabolite analysis of [18F]Florbetaben (BAY 94-9172) in human subjects: a substudy within a proof of mechanism clinical trial. Journal of Radioanalytical and Nuclear Chemistry 284:557-62.

38. Brendel M, Delker A, Rötzer C, et al. (2014) Impact of partial volume effect correction on cerebral β-amyloid imaging in APP-Swe mice using [(18)F]-florbetaben PET. Neuroimage 84:843-53.

39. Cole GB, Keum G, Liu J, et al. (2010) Specific estrogen sulfotransferase (SULT1E1) substrates and molecular imaging probe candidates. Proc Natl Acad Sci U S A 107:6222-7.

40. Lockhart A, Lamb JR, Osredkar T, et al. (2007) PIB is a non-specific imaging marker of amyloid-beta (A ) peptide-related cerebral amyloidosis. Brain 130:2607-15.

41. Kara F, van Dongen ES, Schliebs R, van Buchem MA, de Groot HJM, Alia A (2012) Monitoring blood flow alterations in the Tg2576 mouse model of Alzheimer's disease by in vivo magnetic resonance angiography at 17.6T. Neuroimage 60:958-66.

42. Klunk WE, Lopresti BJ, Ikonomovic MD, et al. (2005) Binding of the positron emission tomography tracer Pittsburgh compound-B reflects the amount of amyloid-beta in Alzheimer's disease brain but not in transgenic mouse brain. The Journal of Neuroscience 25:10598-606.

43. Toyama H, Ye D, Ichise M, et al. (2005) PET imaging of brain with the β-amyloid probe, [11C]6-OH-BTA-1, in a transgenic mouse model of Alzheimer’s disease. Eur J Nucl Med Mol Imaging 32:593-600.

44. Maier FC, Wehrl HF, Schmid AM, et al. (2014) Longitudinal PET-MRI reveals beta-amyloid deposition and rCBF dynamics and connects vascular amyloidosis to quantitative loss of perfusion. Nat Med 20:1485-92.

**Tables**

*Table.1* Overview of scanning protocols.

| Tracer | Mice | Specific Activity (GBq/µmol) | Injected Dose (MBq) | Uptake (min) | Scan time (min) |
|---|---|---|---|---|---|
| **[$^{11}$C]-PiB** | **APPPS1-21 + WT** (n =4, n=4) | 101.14±42.5 | 7.98 ± 0.62 | 60 min dynamic | |
| | **BRI1-42 + WT** (n =5, n=4) | 85.7±12.5 | | | |
| **[$^{18}$F]-FBB** | ***Short uptake*** | | | | |
| | **APPPS1-21 + WT** (n =4, n=5) | 229.4 | 7.5 ± 0.34 | 35 | 15 |
| | **BRI1-42 + WT** (n =5, n=4) | 103.1 | 3.9 ± 0.18 | 35 | 25 |
| | ***Long uptake*** | | | | |
| | **APPPS1-21 + WT** (n =4, n=5) | 175 | 8.1 ± 3.8 | 90 | 15 |

**Figure Captions:**

*Fig.1 Ex-vivo* quantification of total amyloid-β in APPPS1-21 and BRI 1-42 mice. Amyloid-β load was quantified as the % marker stain (JRF/AβN/25 positive) per region and is depicted in a max and min boxplot in graph (a) for APPPS1-21 mice and graph (d) for BRI1-42 mice. Representative immunohistochemical images show the dorsal hippocampus and neighboring cortical region (scale bar = 200 µm) and the cerebellum (scale bar = 20 µm) from APPPS1-21 mice (b),and (c), and BRI1-42 mice (e) and (f).

*Fig.2 In vivo* quantification of amyloid-β. Graphs demonstrate the regional cerebral retention of [$^{11}$C]-PiB and [$^{18}$F]-FBB in APPPS1-21, (a) and (b), and BRI1-42, (c) and (d), mice in comparison to their respective wild-types. Tracer uptake was quantified as the %ID/g and is displayed as the max and min uptake values of an animal group with the mean.

*Fig. 3 In vivo* comparison of amyloid tracer retention. Average images of (a) [$^{11}$C]-PiB uptake and (b) [$^{18}$F]-FBB uptake in APPPS1-21 and BRI1-42 transgenic mice and their respective wild-types. The upper panels of (a) and (b) depict coronal sections whereby the right side of the image corresponds to the left side of the brain and vice versa. The lower panels of (a) and (b) represent sagittal images whereby the right side of the image represents the posterior of the brain. Images are quantified as %ID/g and are overlaid on a $T_2$-weighted MRI template for anatomical reference.

*Fig. 4* (a) Correlation between in vivo retention of [$^{11}$C]-PiB and [$^{18}$F]-FBB in APPPS1-21 and WT mice. Regional uptake values for each animal that underwent both scanning procedures are illustrated. WT are in grey and APPPS1-21 are in white. (b) and (c) depict correlation analysis between *ex vivo* measures of amyloid-β pathology and the *in vivo* μPET signal obtained with [$^{11}$C]-PiB (b) and [$^{18}$F]-FBB (c) in APPPS1-21 mice.

*Fig.5* Percentage difference images obtained for [$^{11}$C]-PiB and [$^{18}$F]-FBB in APPPS1-21 mice versus their WT. Percentage difference was calculated as (TG-WT)/WT*100. Images are overlaid on a $T_2$-weighted MRI template for anatomical reference.

*Fig.6* Representative PET image (1mm Gaussian filtered) from a 90 min uptake of [$^{18}$F]-FBB in an APPPS1-21 mouse overlaid on a C57BL/6J skull CT template. High bone radioactivity is evident. (b) and (c) depict dynamic [$^{11}$C]-PiB PET TAC's (0-200 s) in BRI1-42 and control mice. All data is expressed as the mean.

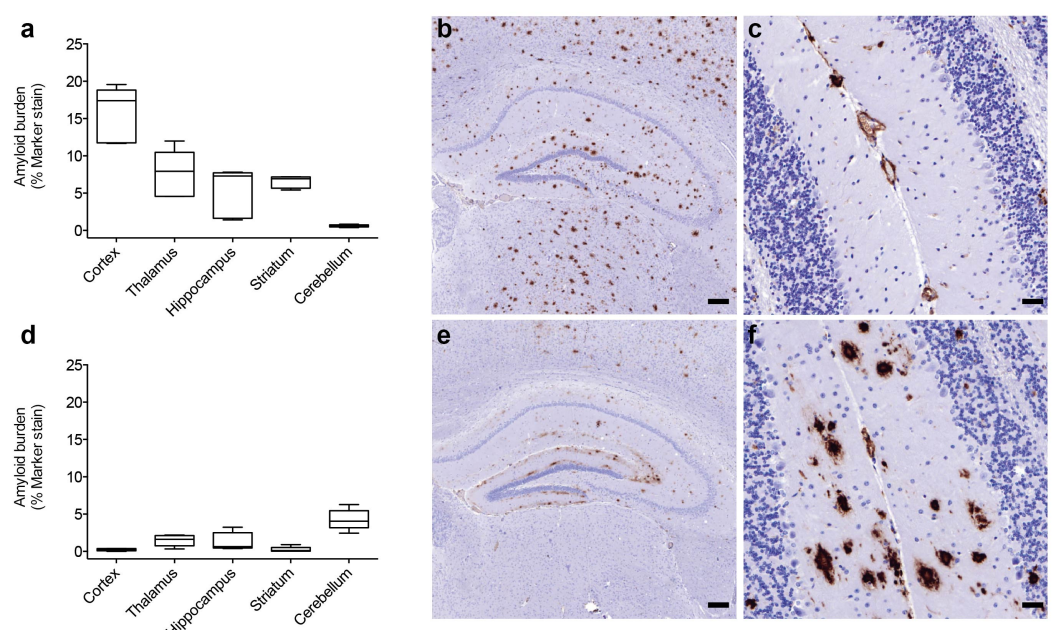
a
Amyloid burden
(% Marker stain)
25
20
15
10
5
0
Cortex
Thalamus
Hippocampus
Striatum
Cerebellum
b
c
d
Amyloid burden
(% Marker stain)
25
20
15
10
5
0
Cortex
Thalamus
Hippocampus
Striatum
Cerebellum
e
f

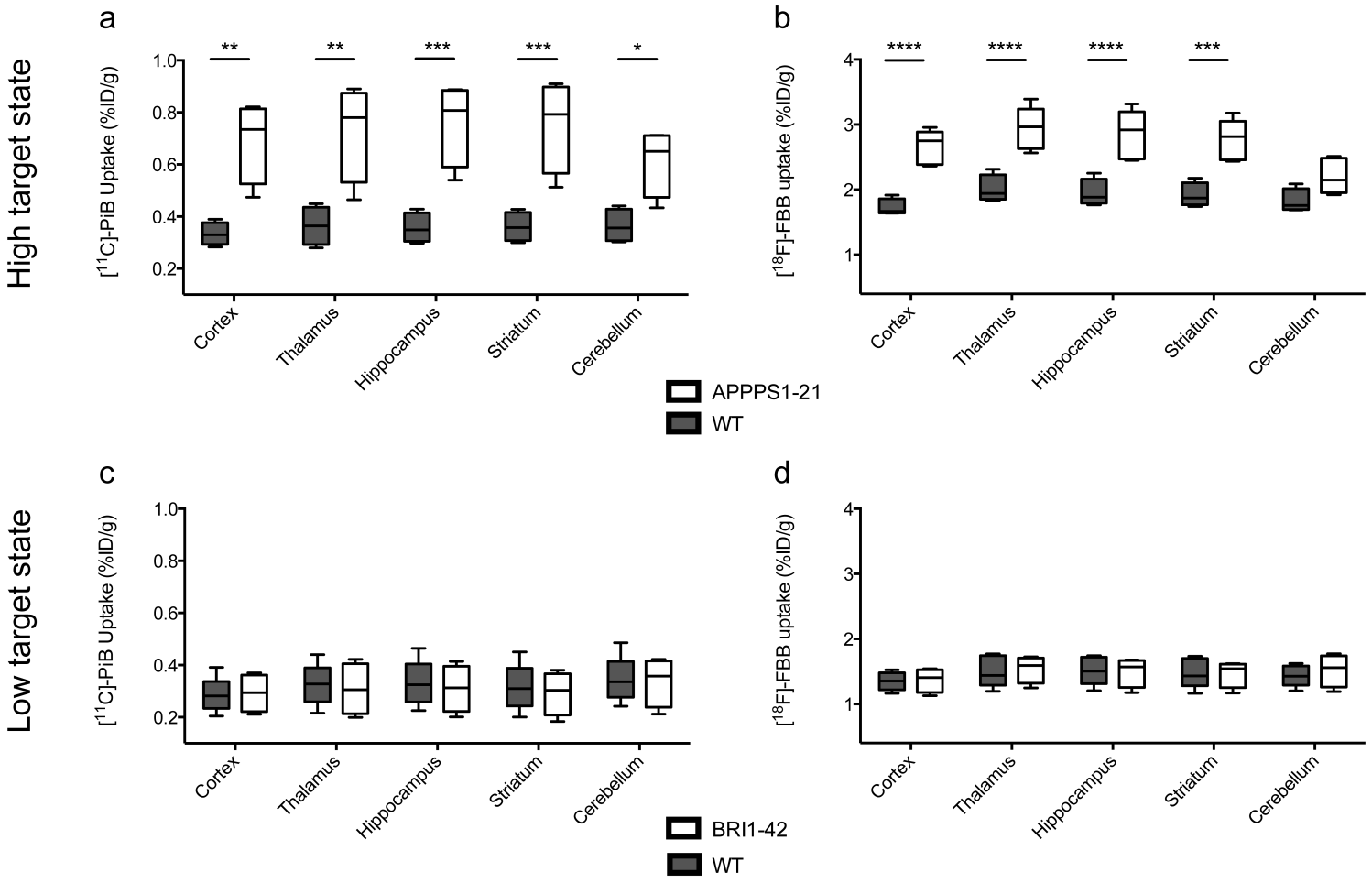
High target state
Low target state
a
b
c
d
[11C]-PiB Uptake (%ID/g)
[18F]-FBB uptake (%ID/g)
Cortex
Thalamus
Hippocampus
Striatum
Cerebellum
APPPS1-21
WT
BRI1-42
WT

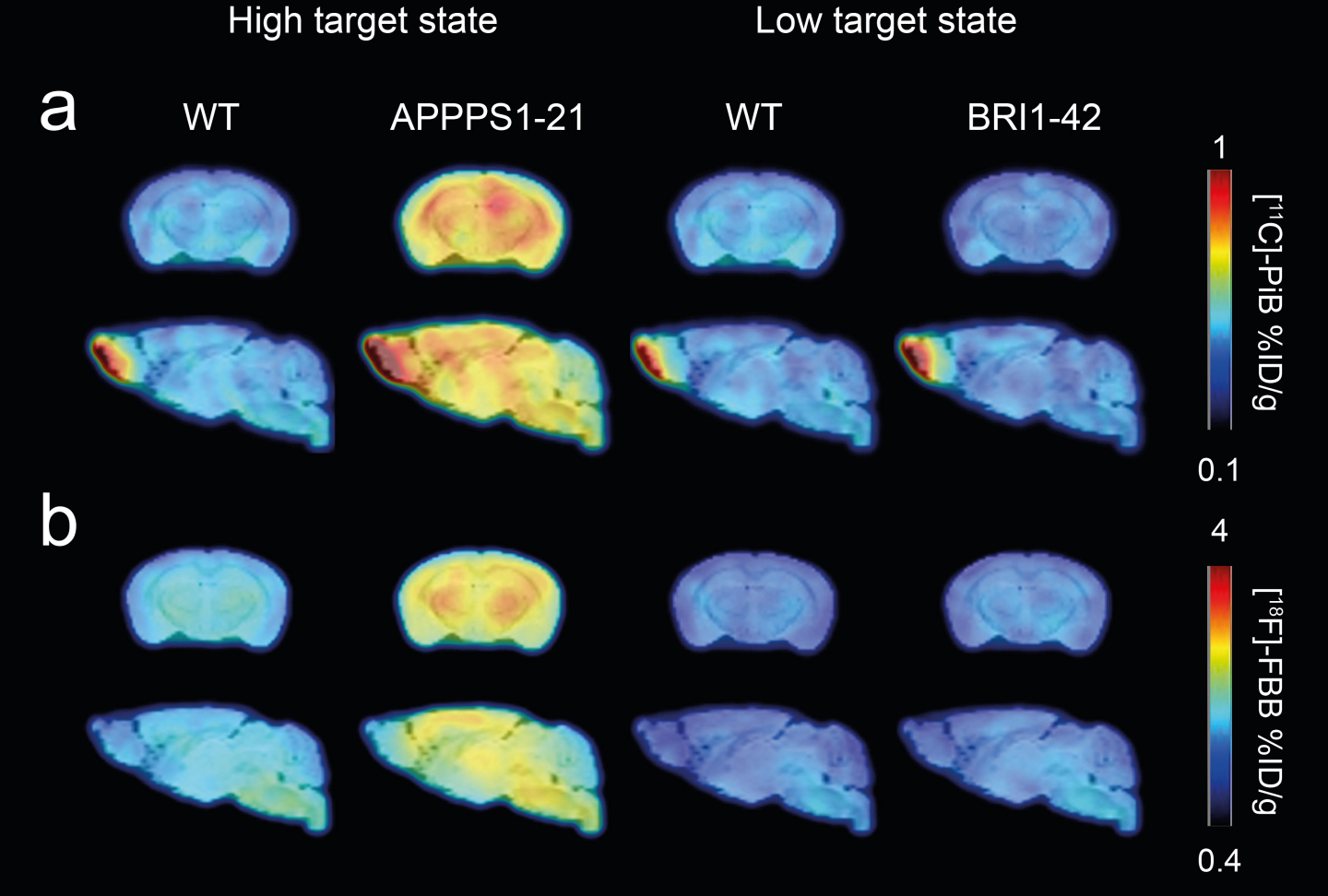
High target state
Low target state
a
WT
APPPS1-21
WT
BRI1-42
1
[11C]-PiB %ID/g
0.1
b
4
[18F]-FBB %ID/g
0.4

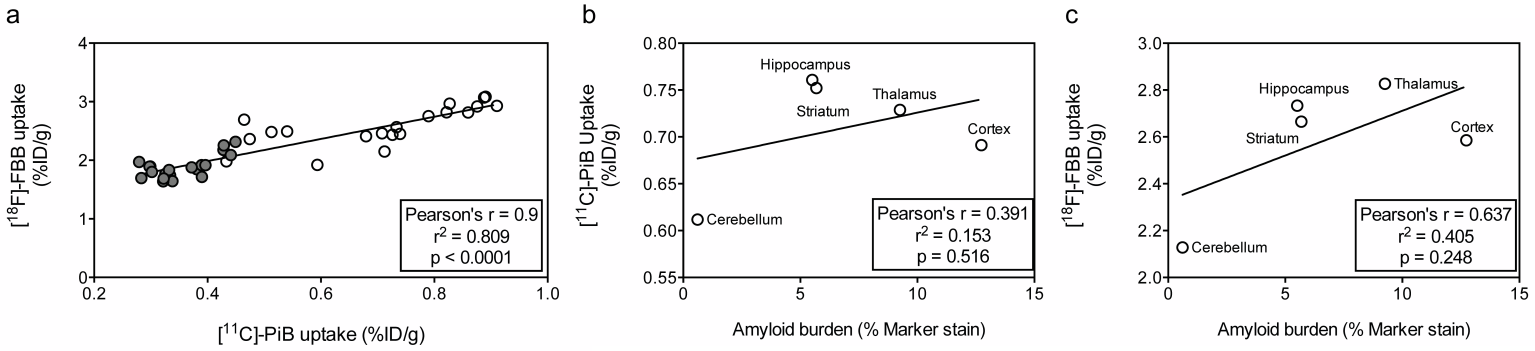
a
[18F]-FBB uptake (%ID/g)
[11C]-PiB uptake (%ID/g)
Pearson's r = 0.9
r2 = 0.809
p < 0.0001
b
[11C]-PiB Uptake (%ID/g)
Amyloid burden (% Marker stain)
Hippocampus
Striatum
Thalamus
Cortex
Cerebellum
Pearson's r = 0.391
r2 = 0.153
p = 0.516
c
[18F]-FBB uptake (%ID/g)
Amyloid burden (% Marker stain)
Hippocampus
Thalamus
Striatum
Cortex
Cerebellum
Pearson's r = 0.637
r2 = 0.405
p = 0.248

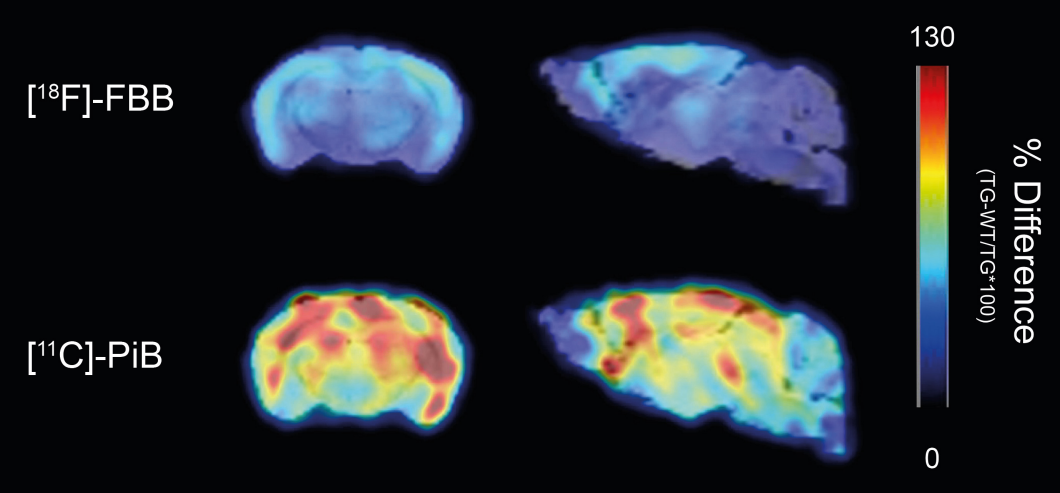
[18F]-FBB
[11C]-PiB
130
0
% Difference
(TG-WT/TG*100)

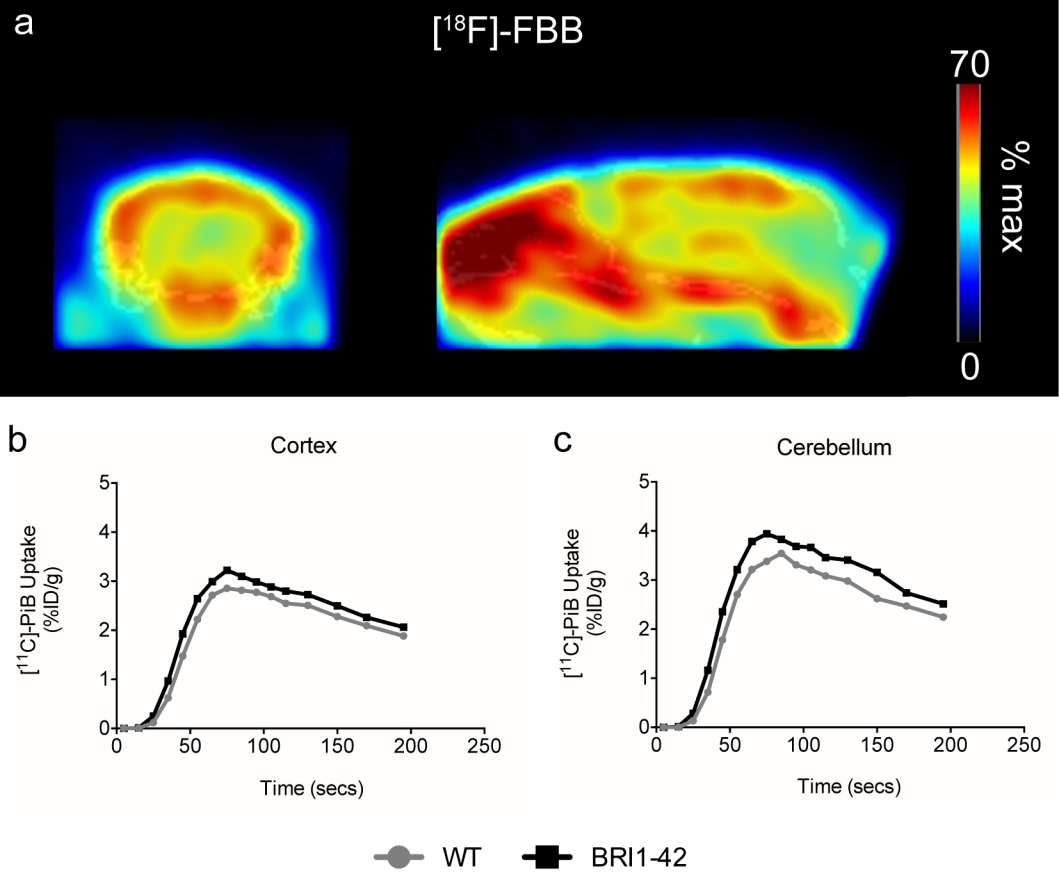
a
[18F]-FBB
70
% max
0
b
Cortex
[11C]-PiB Uptake (%ID/g)
Time (secs)
c
Cerebellum
[11C]-PiB Uptake (%ID/g)
Time (secs)
WT
BRI1-42